IOP PUBLISHING JOURNAL OF MICROMECHANICS AND MICROENGINEERING

J. Micromech. Microeng. **19** (2009) 055012 (13pp) doi:10.1088/0960-1317/19/5/055012

Effect of channel surface wettability and temperature gradients on the boiling flow pattern in a single microchannel

Wei Zhang[1], Guohua Liu[1], Jinliang Xu[1,3] and Yongping Yang[2]

[1] Micro Energy System Laboratory, Guangzhou Institute of Energy Conversion, Chinese Academy of Science, Guangzhou, 510640, People's Republic of China
[2] Beijing Key Laboratory of Energy Safety and Clean Utilization, North China Electric Power University, Beijing, 102206, People's Republic of China

E-mail: xujl@ms.giec.ac.cn

Received 2 January 2009, in final form 8 March 2009
Published 28 April 2009
Online at stacks.iop.org/JMM/19/055012

Abstract
The objective of this paper is to investigate the effects of channel surface wettability and temperature gradients on the boiling flow pattern in a single microchannel. The test section consists of a bottom silicon substrate bonded with a top glass cover. Three consecutive parts of an inlet fluid plenum, a central microchannel and an outlet fluid plenum were etched in the silicon substrate. The central microchannel had a width of 800 μm and a depth of 30 μm. Acetone liquid was used as the working fluid. High outlet vapor qualities were dealt with here. The flow pattern consists of a fluid triangle (shrinkage of the liquid films) and a connected long liquid rivulet, which is generated in the central microchannel in the timescale of milliseconds. The peculiar flow pattern is formed due to the following reasons: (1) the liquid rivulet tends to have a large contact area with the top hydrophilic channel surface of the glass cover, but a smaller contact area with the bottom silicon hydrophobic surface. (2) The temperature gradient in the chip width direction at the top channel surface of the glass cover not only causes the shrinkage of the liquid films in the central microchannel upstream, but also attracts the liquid rivulet populated near the microchannel centerline. (3) The zigzag pattern is formed due to the competition between the evaporation momentum forces at the vapor–liquid interfaces and the force due to the Marangoni effect. The former causes the rivulet to deviate from the channel centerline and the latter draws the rivulet toward the channel centerline. (4) The temperature gradient along the flow direction in the central microchannel downstream causes the breakup of the rivulet to form isolated droplets there. (5) Liquid stripes inside the upstream fluid triangle were caused by the small capillary number of the liquid film, at which the large surface tension force relative to the viscous force tends to populate the liquid film locally on the top glass cover surface.

(Some figures in this article are in colour only in the electronic version)

1. Introduction

Boiling heat transfer in microsystems is important because it involves many engineering applications, such as electronic cooling at high heat flux (Thome 2004), thermal control of fuel cells (Garrity *et al* 2007) and microthruster force generation for micro/nano satellites (Maurya *et al* 2005). Kandlikar *et al* (1997) investigated the flow over a bubble attached to a channel wall at a given contact angle and gave a bubble nucleation criterion, representing the lowest temperature at which a cavity of a given size works as nucleation site. These cavities will continue to nucleate at higher superheats as seen in their plotting curves. If the cavities of this radius are not available, the onset of nucleation will be delayed into the

[3] Author to whom any correspondence should be addressed.

channel downstream until the wall superheat meets the bubble nucleation criterion. If the onset of nucleation occurs over cavities of radius 3 μm, the minimum wall superheat required to initiate should be 15 °C with saturated water in a 1054 × 97 μm channel with a mass flux of 120 kg m^{-2} s^{-1} and a heat flux of 300 kW m^{-2}. Kandlikar *et al* (2006) pointed out that the wall superheats at the onset of nucleate boiling (ONB) are quite high in microchannels, even in the presence of the right sized cavities.

The high wall and liquid superheats in microchannels cause the rapid bubble growth and flow reversal, leading to two-phase flow instabilities. The boiling flow instability not only causes an uneven thermal stress on the heating surface, but also leads to an early appearance of critical heat flux (CHF). Thus, it is a notable problem if not addressed properly (Kuo and Peles 2008). It was found that several experimental works evidenced these instabilities meanwhile only very limited theoretical developments exist in the literature (Tadrist 2007). Several research groups such as Qu and Mudawar (2004), Wu *et al* (2006), Hetsroni *et al* (2006), Kandlikar *et al* (2006) and Muwanga *et al* (2007) studied the two-phase flow instabilities. Recent progress in this area also includes the mitigation of the boiling flow instability in microchannels.

Other factors, such as channel surface wettability and temperature gradients, also influence the flow and heat transfer performance. Recently, Hsieh and Lin (2009) studied convective heat transfer in liquid microchannels with hydrophobic and hydrophilic surfaces. Regarding the temperature gradient issue in microsystems, Takahashi *et al* (1999) analyzed the Marangoni effect due to the temperature gradients on the droplet or bubble movements in microsystems. A recent paper by Zhang *et al* (2008a) studied the Marangoni effect on the bubble movements in three parallel microchannels. It was found that a small temperature difference across the channel width results in a large temperature gradient in that direction, attracting bubbles in the two side channels to approach the center microchannel. Both surface wettability and temperature gradients influence the vapor and liquid phase distribution in microsystems, but they are less reported in boiling microsystems.

We studied the combined effects of channel surface wettability and temperature gradients on the vapor and liquid phase distribution in boiling microchannels. In order to do that, a silicon chip was fabricated consisting of a bottom silicon substrate bonded with a top 7740 Pyrex glass cover. Along the flow direction, three consecutive parts of an inlet fluid plenum, a central microchannel and an outlet fluid plenum were included. Acetone liquid was used as the working fluid. The tests were performed at high outlet thermal equilibrium vapor qualities. The periodic rivulet ejection and receding pattern was observed. The channel surface wettability and temperature gradients were used to explain the flow pattern formation. The flow pattern details influenced by parameters such as mass flux and heat flux were also discussed. The flow pattern strongly influenced the heat transfer in the microchannel heat sink, under a nearly dry-out condition.

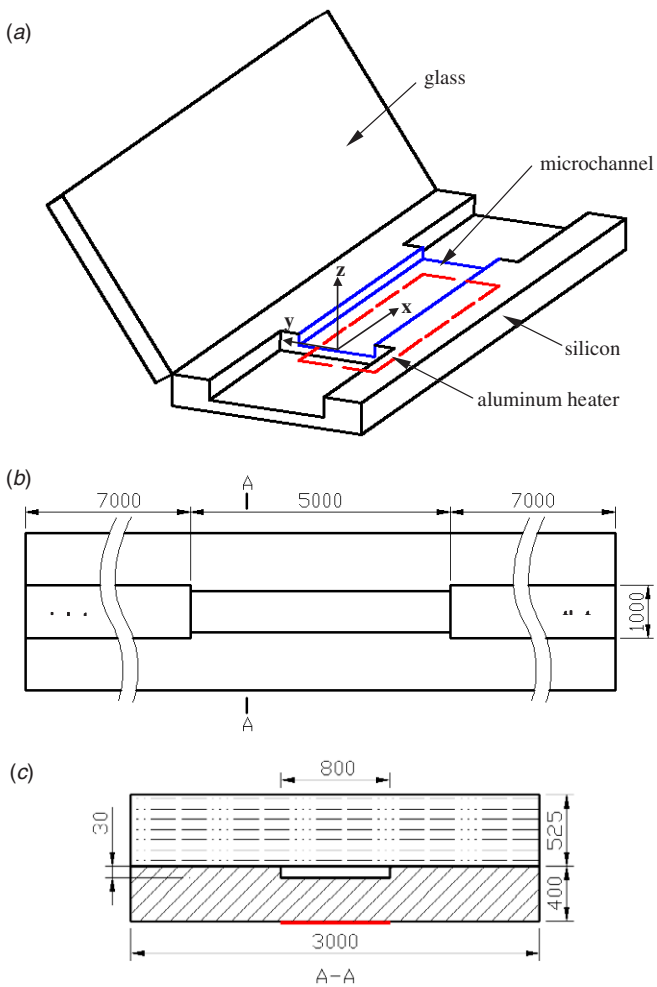

Figure 1. The silicon microchannel heat sink used in the present study (all dimensions are in μm).

2. Test section and experimental apparatus

2.1. Silicon microchannel test section

It is well known that deep microchannels have a large surface area to volume ratio; thus they are recommended in the heat transfer engineering. However, flow visualization in deep microchannels is quite difficult (Zhang *et al* 2008b). If a deep microchannel is rotated by 90°, the channel width and depth are interchanged and a wide, shallow channel results. The present silicon chip is designed based on this idea. Therefore, bubble dynamics and flow patterns can be easily achieved by analyzing a set of recorded images.

Figure 1 shows the microchannel test section, consisting of a top 7740 Pyrex glass cover and a silicon substrate, with a thickness of 525 μm and 400 μm, respectively. In the silicon substrate, three consecutive zones were etched along the flow direction (see figure 1(*b*)): an inlet plenum (acting as an inlet header), a central microchannel and an outlet plenum (acting as an outlet header). Both the inlet and outlet plenums had a 1000 μm wide and 120 μm deep cross section. The central microchannel had a length of 5000 μm with a rectangular cross section of 800 μm width and 30 μm depth. It had a large width

to depth ratio of 26.7. Figure 1(*c*) shows the cross section of the central microchannel.

An aluminum film with a thickness of 5000 Å was deposited at the back surface of the silicon substrate by the low-pressure chemical vapor deposition (LPCVD) technique, acting as the heating source for the heat transfer system. The thin aluminum film had a length of 5000 μm and a width of 800 μm, exactly corresponding to the planar area of the central microchannel. A dc power source supplied the thin heating film (not shown in figures 1 and 2). The heating power on the aluminum film was obtained by measuring the voltage across the thin heating film and current flowing through the thin heating film. The three microchannel parts were fabricated by the ICP dry etching technique. In order to characterize the flow behavior in the central microchannel, a three-coordinate system was established (see figure 1(*a*)). The axial flow coordinate x starts from the central microchannel entrance. The channel width is referred to as the y coordinate with $y = 0$ at the microchannel centerline. The channel depth is referred to as the z coordinate with $z = 0$ representing the bottom surface of the central microchannel.

2.2. Experimental setup and procedure

The experimental setup is shown in figure 2. A forced convection loop was built up with three subsystems: the liquid supply system, the silicon chip test section and the optical measurement system and the liquid collection system. The liquid supply system consists of a nitrogen gas bottle, a precision pressure regulator, a liquid tank and a constant temperature control unit. Liquid acetone in the tank, with a temperature control uncertainty of 0.5 °C by the PID temperature control unit, is pressurized by high-pressure nitrogen gas and flows successively through a 2 μm filter and the silicon chip. The two-phase mixture (alternatively, the superheated vapor) leaving the silicon chip was condensed in a condenser (heat exchanger) and the condensed liquid was collected by a glass beaker, which was located on the top surface of a high-precision electronic balance.

The inlet and outlet fluid temperatures (T_{in} and T_{out}) were measured by high-precision K-type jacket thermocouples. The condensed liquid was measured by an electronic balance with an accuracy of 0.02 g. The mass flow rate was calculated by the increased liquid weight over a given period of time. The inlet pressure (p_{in}) was measured by a Setra pressure transducer (model 206). The pressure drop across the silicon chip (Δp) was measured by a Senex differential pressure transducer. The pressure and temperature signals were recorded by a high-speed data acquisition system (DL 750, Yokogawa, Inc., Japan) with 16 channels. While a data sampling rate up to 10 million points per second is possible with this system, in the present study, the recording rate was selected as 100 samples per second, which is fast enough to match the response time of the pressure and temperature signals.

Transient flow patterns in the central microchannel (800 μm width and 30 μm depth) but not limited to the central microchannel were observed by our joined optical system. The microscope is a Leica M stereo microscope (Germany). A powerful cold light source (Schott-kl 1500 LCD, Germany) was used to receive a clear image when the microscope is running. The light source has a power of 150 W at a dc voltage of 15 V. It has a wavelength of 430–490 nm. Heat received by the silicon chip from the cold light source is less because most of energy transported by radiation takes place in the infrared region with a wavelength of 0.76–20 μm (Howell and Menguc 1998). Chen and Garimella (2006) show that the cold light source almost had no influence on the test section. The microscope is connected with a high-speed camera system (Redlake, Inc., USA) with a 1 inch C-type port. The high-speed camera system has a maximum recording rate of 20 000 frames per second with a resolution of 1504 × 1128 pixels. High recording rates need a very powerful light source. In this study, a high-speed recording rate of 5000 frames per second was used. The flow visualization view area was mainly focused on the central microchannel. But the inlet and outlet fluid plenums were also included.

A thin black lacquer was painted on the back surface of the silicon chip. The heating surface temperature at the back silicon surface was measured by a high-resolution high-accuracy infrared radiation image system (FLIR ThermaCAM SC3000 IR). The thermal sensitivity at the room temperature is 0.02 °C with a typical resolution of 320 × 240 pixels over the whole heating area (5000 μm length and 800 μm width). Thus the spatial resolution for the IR image system was about 36 μm. The IR image camera ensures the precise determination of not only the maximum temperature but also the temperature gradients on the heating surface. It is noted that the surface temperatures measured by the IR image system were also reported by Hetsroni *et al* (2006).

It is noted that the temperatures of the glass cover surface are important to describe the flow boiling phenomena in microchannels. However, measurement of the temperatures is difficult at this stage. The glass cover surface is bright so that it has a low emissivity. Coating a thin black lacquer on the glass cover surface for the temperature measurement by an IR image system makes the measurement of the flow pattern in microchannels impossible. Attaching thermocouples on the glass cover surface is not preferable because this method cannot achieve the temperature variations on the glass cover surface corresponding to the microchannel, especially in the chip width direction.

2.3. Data reduction and parameter uncertainties

The liquid used in this study was pure acetone (CH_3COCH_3, molecular weight of 58.08, purity larger than 99.5%). The major physical properties are shown in table 1, cited from Yaws (1999). It is noted that the surface tension force decreased with the increase in temperatures for acetone: $\sigma = 62.2 \times 10^{-3}\,(1 - T/508.2)^{1.124}$ in the units of N m^{-1}; note that the unit of temperature (T) is K. The data reduction process involves determinations of the mass flux G, the heat flux q, the boiling number Bo and the outlet equilibrium vapor qualities x_{out}.

The mass flux G was defined as the total mass flow rate (m) over the cross-sectional area of the central microchannel,

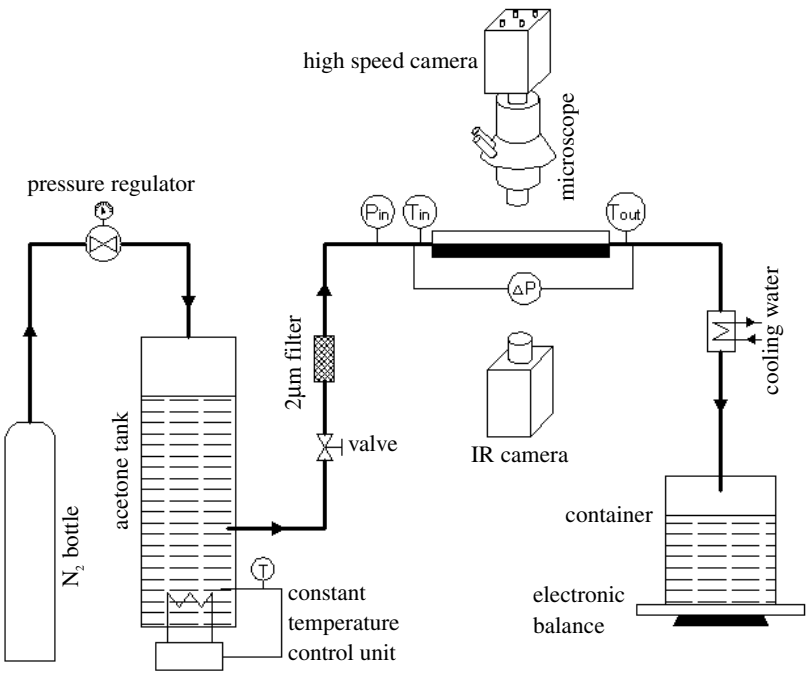

Figure 2. The experiment setup.

Table 1. Major physical properties of acetone at atmospheric pressure.

T_{sat} (°C)	ρ_f (kg m^{-3})	ρ_g (kg m^{-3})	M_w (g mol^{-1})	C_{pf} (J kg^{-1} K^{-1})	C_{pg} (J kg^{-1} K^{-1})	h_{fg} (kJ kg^{-1})	μ_f (Pa s)	μ_g (Pa s)	k_f (W mK^{-1})
56.3	748.0	1.71	58.1	2302.5	1380.6	512.94	2.37×10^{-4}	8.31×10^{-6}	0.168

Note: T_{sat} is the saturation temperature, ρ_f and ρ_g are the densities of liquid and vapor, M_w is the molecular weight, C_{pf} and C_{pg} are the specific heat of liquid and vapor, μ_f and μ_g are the viscosities of liquid and vapor and k_f is the thermal conductivity of liquid.

$G = m/A_c$, where A_c is the cross-sectional area of the central microchannel.

The heat flux q at the film heater area (5000 × 800 μm) was calculated by $q = \phi VI/(L_{film} W_{film})$, where ϕ is the thermal efficiency, which is the ratio of heat received by the fluid to the total heating power, V and I are the voltage and current for the thin film heating, L_{film} and W_{film} are the length and width of the thin film heater, respectively.

The boiling number Bo is defined as $Bo = q/(Gh_{fg})$, where h_{fg} is the latent heat of evaporation.

The outlet equilibrium vapor quality x_{out} is defined as $x_{out} = (h_{out} - h_f)/h_{fg}$, where h_{out} is the exit fluid enthalpy and h_f is the saturated liquid enthalpy corresponding to the exit atmospheric pressure. h_{out} is determined based on the energy conservation equation $m(h_{out} - h_{in}) = \phi VI$.

It is noted that the vapor quality is defined based on the thermodynamic equilibrium point of view. The equilibrium vapor quality x_{out} is negative for the subcooled liquid, showing the degree that the liquid deviates from the saturated liquid state. In the two-phase region, x_{out} is in the range from zero to unity. For the superheated vapor, x_{out} must be larger than unity, showing the degree that the superheated vapor deviates from the saturated vapor state. In the present study, the mass flow rate is small and the silicon chip has temperatures significantly larger than the saturation temperature of acetone. The thermal equilibrium vapor quality larger than unity means the superheated vapor state at the end of the central microchannel. However, the strong thermal non-equilibrium effect is apparent, i.e., the superheated vapor and liquid triangle or rivulet co-exist in the central microchannel, which will be seen later.

2.4. Uncertainty analysis

The pressure drop transducer has an accuracy of 0.1% with a response time of 0.1 s. The used thermocouples have an accuracy of 0.3 °C with a response time of 0.01 s. The flow rate uncertainty is 1.0%. The IR imaging system has a temperature uncertainty of 0.5 °C with a response time of 0.25 s. Performing the standard error analysis yields uncertainties of mass flux of 1.5%.

Heat loss of the microsystem includes radiation and natural convection heat transfer from the heated chip surface to environment. Heat loss also includes thermal conduction from the microsystem to its upstream and downstream connection tubes. A set of single-phase liquid flow experiments were performed. The thermal efficiency ϕ was calculated by the heat received by acetone liquid (calculated from mass flow rate and inlet/outlet fluid temperature differences) divided by the total applied heating power. The calibrations identified a highest thermal efficiency of 0.72 and a smallest value of

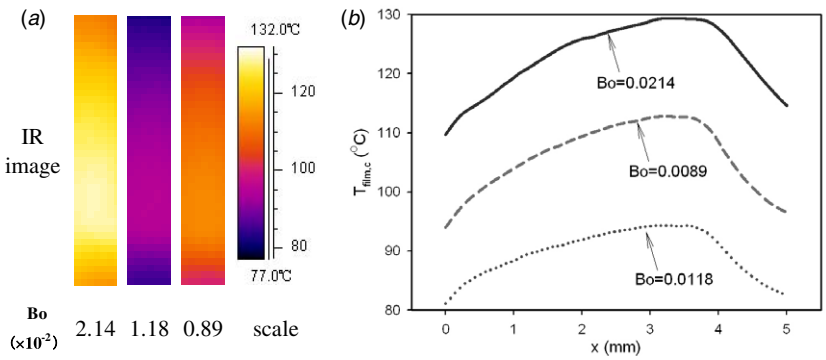

Figure 3. IR images showing the bottom heating surface temperatures (*a*), and the heating surface temperatures at the centerline of $y = 0$ (*b*), for the three runs.

Table 2. Run parameters used in the present study.

Run	G (kg m^{-2} s^{-1})	Δp (kPa)	T_{in} (°C)	T_{out} (°C)	q (kW m^{-2})	x_{out}	*Bo*
1	28.7	20.42	33.0	68.0	319.4	3.56	0.0214
4	43.9	20.18	27.8	59.5	269.7	1.95	0.0118
6	78.1	30.12	30.7	67.3	363.0	1.47	0.0089

0.61. Thus, we selected an average value of 0.66, under which the maximum uncertainty of ϕ is 5%. Given the fact that the voltage measurement is very accurate (the DL750 data acquisition system has an error of 0.1 mV for the voltage measurement), this estimation of ϕ directly leads to the uncertainty of heat flux of 5.0%.

Many factors influence the effective thermal efficiency. However, from the single-phase liquid flow experiment, it is found that the major parameters influencing the effective thermal efficiency ϕ are the applied heating power and heating surface temperature. The mass flow rates for the single-phase liquid flow are quite smaller than those for the two-phase flow, and the heat transfer coefficients inside the microchannel for the single-phase liquid flow are smaller than those for the two-phase flow. By adjusting the mass flow rate during the calibration experiment, one can obtain a similar heating surface temperature with that for a two-phase flow experiment when the same heating power is applied. In this way the effective thermal efficiency for the single-phase flow is roughly identical to that for the two-phase flow experiment. The calibration experiments maintain the similar ranges of applied heating power and heating surface temperature with those to two-phase flow.

3. Results and discussion

The objective of this study is to investigate the flow and heat transfer characteristics at high outlet vapor qualities. A set of experiments were performed, with the following data ranges: mass flux G of 28–100 kg m^{-2} s^{-1}, heat flux q of 170–420 kW m^{-2}, outlet fluid temperature T_{out} of 57–68 °C and outlet thermal equilibrium vapor quality x_{out} of 1.09–3.56.

For each run, we maintained the pressure drop across the silicon chip at a fixed value such as 20 kPa, 30 kPa, etc. The heating power was applied on the back aluminum film surface step by step. The heating surface temperature was tracked by the IR image system. A single-phase liquid flow existed in the microchannel system for the negative wall superheats. Further increase in heat fluxes at the back heating surface resulted in significant wall superheat, i.e. $\Delta T_{sup} = T_{film} - T_{sat} > 0$. Boiling incipience was triggered initially in the outlet fluid plenum (see figure 1). Then the boiling two-phase flow propagates to the central microchannel and the inlet fluid plenum, leading to the significantly decreased flow rate. The common flow pattern observed in the 30 μm microchannel is the periodic rivulet ejection and receding. However, depending on different heat flux and mass flux, the flow details may be slightly varied. It was found that the temperature variations in the x-, y-, z-directions affect the flow behavior. Thus we show the back heating surface temperatures measured by the IR image system in figure 3(*a*) for the boiling numbers of 0.0214, 0.0118 and 0.0089, corresponding to runs of 1, 4 and 6, respectively (see table 2). Run 1 had the highest temperatures and run 4 had the lowest temperatures. The heating surface temperatures at the centerline of $y = 0$, i.e., $T_{film,c}$, are shown in figure 3(*b*) for the three runs. The temperatures increased, reached the maximum and then decreased versus x along the flow direction.

3.1. The periodic liquid rivulet ejection and receding pattern

3.1.1. The flow pattern. In this study, we found that inlet and outlet fluid temperatures (T_{in} and T_{out}) and pressure drop (Δp) did not change versus time even though the observed flow patterns were dynamically evolved in the timescale of milliseconds. This is true for all runs described in this study. This is due to the size of the pressure and temperature sensors used, which have the response time of 0.1 s and 0.01 s, respectively. The two sensors may not capture the fast dynamic change of the flow and heat transfer behavior of the silicon chip. Thus they gave the stable signal output versus time. Run 1 is selected for the flow pattern demonstration and analysis

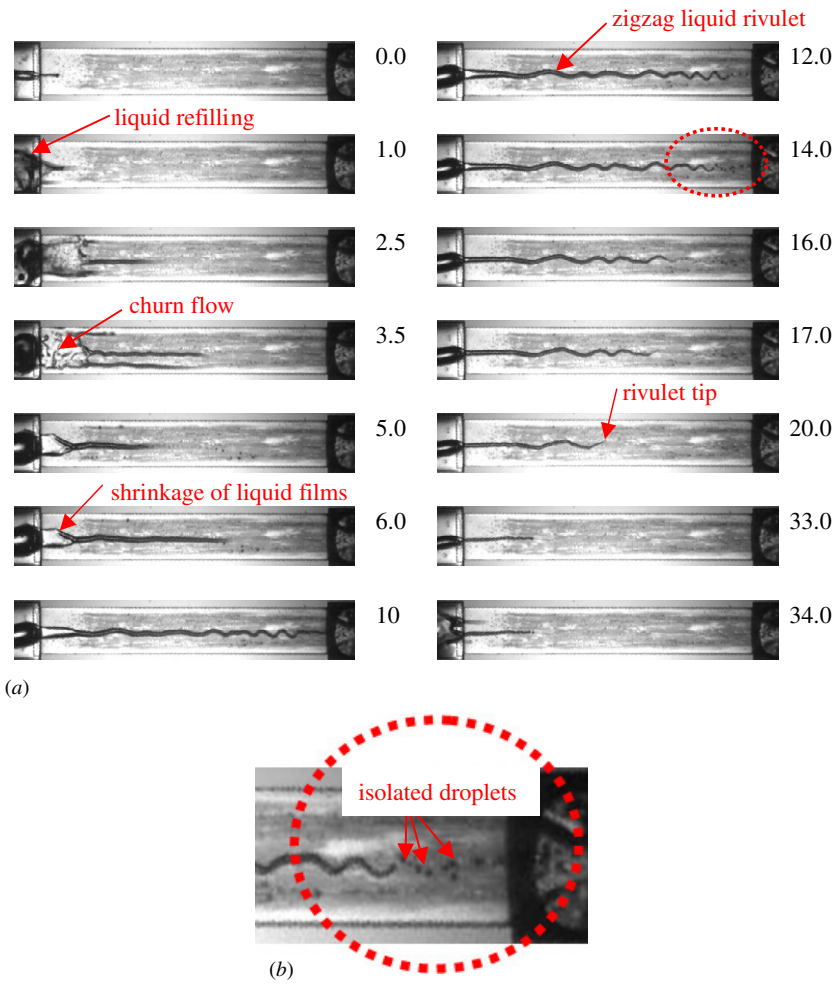

Figure 4. Periodic liquid rivulet ejection and receding process (*a*), and the enlarged image showing isolated droplets formed by the breakup of the rivulet (*b*), for run 1 (time scale is millisecond).

with $T_{in} = 33$ °C, $T_{out} = 68$ °C, $\Delta p = 20.42$ kPa, $G = 28.7$ kg m^{-2} s^{-1} and $q = 319.4$ kW m^{-2} (see table 2). Figure 4(*a*) shows the periodic liquid rivulet ejection and receding pattern. A new cycle begins when there is a liquid thread in the inlet fluid plenum, but the whole central microchannel is almost full of vapor (see the image at $t = 0$ in figure 4(*a*)). The tip of the liquid thread (rivulet) penetrates the junction interface of the inlet fluid plenum and the central microchannel at $t = 1.0$ ms in figure 4(*a*). Then a churn (chaotic) mushroom cloud, containing a mixture of vapor and liquid, was ejected into the central microchannel. A planar fluid triangle (shrinkage of liquid films), consisting of two contracted liquid films and the mixture of vapor and liquid inside, appears in the central microchannel upstream (see the images for $t > 5.0$ ms in figure 4(*a*)).

In order to identify the complicated fluid structure inside the upstream fluid triangle, we performed the air–water two-phase flow to identify the image characteristics. Initially, the three consecutive microchannels along the flow direction are filled with air because they are connected with the environment through the connection tube. Then the liquid water is pumped slowly into the microchannel. It is found that the white part of the image always represents the vapor phase, while the black part of the image shows the liquid phase. Therefore, the flow structure inside the upstream fluid triangle is the vapor–liquid mixture for $t < 5.0$ ms, and vapor at $t = 5.0$, 6.0 and 10.0 ms (see figure 4). In the following section, we note that liquid stripes are observed inside the upstream fluid triangle.

The shrinkage of the two liquid films, identified by the images for 5.0 ms $< t <$ 16.0 ms, is caused by the temperature gradient in the y-direction on the top channel surface (glass cover), which will be explained later. In front of the fluid triangle there is a long liquid rivulet populated near the microchannel centerline with the zigzag pattern. The rivulet reached the end of the central microchannel at $t = 10.0$ ms as shown in figure 4(*a*). For the time $t > 12.0$ ms, the rivulet was broken in the central microchannel downstream to form isolated droplets (see the circled image at $t = 14.0$ ms in figure 4(*a*)). The tip of the rivulet is being receded to the central microchannel upstream due to evaporation for $t > 12.0$ ms in figure 4(*a*), until the whole central microchannel is almost dry out, leaving a short rivulet in the central microchannel upstream (see the images at $t = 33.0$ and 34.0 ms in figure 4(*a*)). Then a new rivulet ejection and receding cycle starts. Figure 4(*b*) shows the enlarged image for the isolated droplets formed by the breakup of the rivulet.

In order to demonstrate the periodic rivulet ejection and receding process, we plotted the axial coordinate x for the rivulet tip versus time in figure 5(*a*). The curve indeed displays the cycle behavior. During each cycle, the rivulet tip had a sharp increase of x versus time t, indicating the rivulet ejection process. It reached the maximum value of $x = 5.0$ mm at the end of the central microchannel. Then the axial coordinate of the rivulet tip is decreased versus time, representing the rivulet receding process. The rivulet ejection process is governed by the rivulet ejection momentum from the pumping pressure, and the receding process is governed by the evaporation heat transfer at the rivulet interface. The rivulet ejection velocity, which is the slope of the coordinate x of the rivulet tip with respect to time t, is about 1 m s^{-1}. But the rivulet receding velocity is about 0.25 m s^{-1}, which is smaller than the ejection velocity. Figure 5(*b*) shows the cycle periods versus consecutive cycles, showing that cycle periods are somehow different for different cycles. The longest cycle period attains 83 ms but the shortest one reaches 16 ms, indicating uncertainties of the rivulet ejection and receding speeds for different cycles at high outlet vapor qualities.

3.1.2. The temperature distribution of the silicon chip. Figures 6 and 7 are helpful for explaining the periodic rivulet ejection and receding processes. Figure 6(*a*) shows the liquid rivulet in the central microchannel. Meanwhile, figure 6(*b*) shows temperature distribution at the back heating surface (5000 μm length and 800 μm width) by the IR imaging system, exactly corresponding to the bottom microchannel surface. Because the back heating surface temperatures have negligible gradient in the chip width direction (y-direction), we plot the back heating surface temperatures at the centerline at $y = 0$, i.e. $T_{\mathrm{film,c}}$, along the axial flow direction x. It is seen that the heating wall superheats are significant; note that the saturation temperature of acetone is 56.3 °C at atmospheric pressure. The temperatures are increased from the central microchannel entrance to reach the maximum values at $x =$ 3–4 mm. Then they are decreased in the central microchannel downstream due to the axial thermal conduction of the silicon substrate.

Figure 7(*a*) shows the cross section of the central microchannel, which is formed by the top channel surface (glass cover), two silicon side walls and one bottom silicon wall. The glass cover surface is hydrophilic but the three silicon surfaces are hydrophobic. Thus the cross section of the liquid rivulet has a large contact area with the top channel surface (glass cover), but smaller contact area with the bottom silicon surface. As noted previously, the bottom microchannel surface has negligible temperature gradient in the y-direction. In order to explain the shrinkage of the two liquid films in the central microchannel upstream, and the centerline population of the long rivulet in front of the upstream fluid triangle, we estimate the temperature variations on the top glass cover. Numerical simulation was performed using the commercial software FLUENT 6.0 package. The calculations were performed for the inlet liquid velocity of 0.038 m s^{-1} (mass flux of 28.6 kg m^{-2} s^{-1}) and $T_{\mathrm{in}} = 33$ °C at the entrance of the inlet fluid plenum. The heat flux at the back heating surface (5000 μm length and 800 μm width) was $q = 319.4$ kW m^{-2}. Other surfaces exposed in the air environment had an air natural convection heat transfer coefficient of 10.0 W mK^{-1}. The air temperature was set at the room temperature of 25 °C. The outlet boundary condition had the atmospheric pressure at the end of the outlet fluid plenum. Both the Pyrex glass cover and the etched silicon substrate were considered. The fluid flow in the etched structures was conjugated with the thermal conduction of both the solid silicon and glass cover. It is noted that fluid in the inlet fluid plenum, central microchannel and outlet fluid plenum consecutively had the state of liquid, vapor–liquid mixture and superheated vapor. Heat transfer coefficients are calculated based on these different fluid states. For the two-phase heat transfer coefficient, Chen (1963) proposed a very successful correlation. The proposed correlation covers both the 'saturated nucleate boiling region' and the 'two-phase forced convection region'. It was assumed that both mechanisms occur to some degree over the entire range of the correlation and that the contributions made by the two mechanisms are additive. The detailed calculation procedure can be found in Chen (1963). For the present case, the two-phase heat transfer coefficient is calculated to be 18 kW m^{-2} K^{-1}. The heat transfer coefficients for other runs are also calculated based on the Chen (1963) correlation. The calculated temperatures at the back heating surface are generally in agreement with the measured IR values. Figure 7(*b*) shows the temperature distributions within the cross sections of $x = 1.0$ mm and 4.0 mm. Figure 7(*c*) shows the temperatures at the bonding surface, which reach 123–125 °C outside of the central microchannel. Temperatures at the top channel surface (glass cover) inside the central microchannel are decreased from $y = 400$ μm to $y = 0$ and display a parabolic shape. The average temperature gradient from $y = 400$ μm to $y = 0$ reaches 58 K mm^{-1} at $x = 1.0$ mm. It attains 20 K mm^{-1} at $x = 4.0$ mm, which is smaller than that at $x = 1.0$ mm.

3.1.3. Explanation of the observed flow pattern.

Shrinkage of liquid films in the central microchannel upstream. It is easy to understand the formation of the shrinkage of liquid films in the central microchannel upstream from figure 7. First, the top channel surface (glass cover) is hydrophilic; thus liquid tends to contact with the top microchannel surface. Second, the high-temperature gradient on the top microchannel surface in the y-direction results in a strong Marangoni effect. Liquids tend to move to the center of the microchannel where the temperature is lower than elsewhere, forming the shrinkage of liquid films and the corresponding fluid triangle in the central microchannel upstream. The shrinkage of liquid films here is similar to the phenomenon for the falling liquid films on a heated surface such as the one reported in Zhang *et al* (2007). Due to the same reason, the long liquid rivulet populates near the microchannel centerline.

Zigzag pattern of the long liquid rivulet. The zigzag pattern of the liquid rivulet is caused by the oscillating movement of the rivulet against the channel centerline. Deviation of the

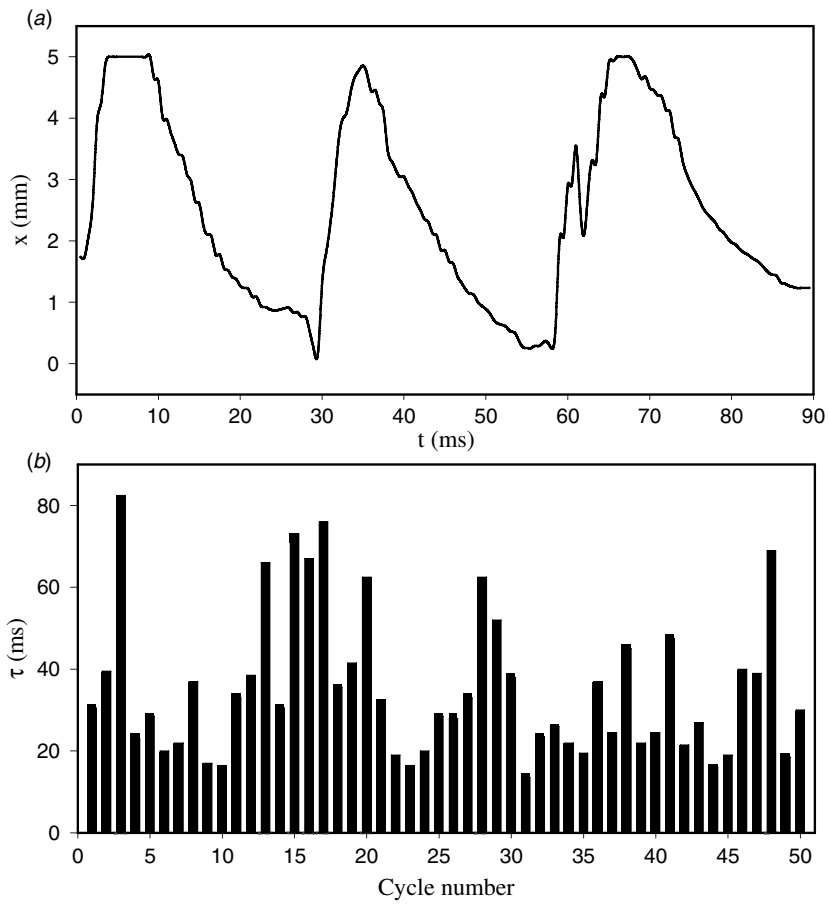

Figure 5. Displacement of the rivulet tip (*a*), and cycle periods of the periodic rivulet ejection and receding process for consecutive cycles (*b*), for run 1.

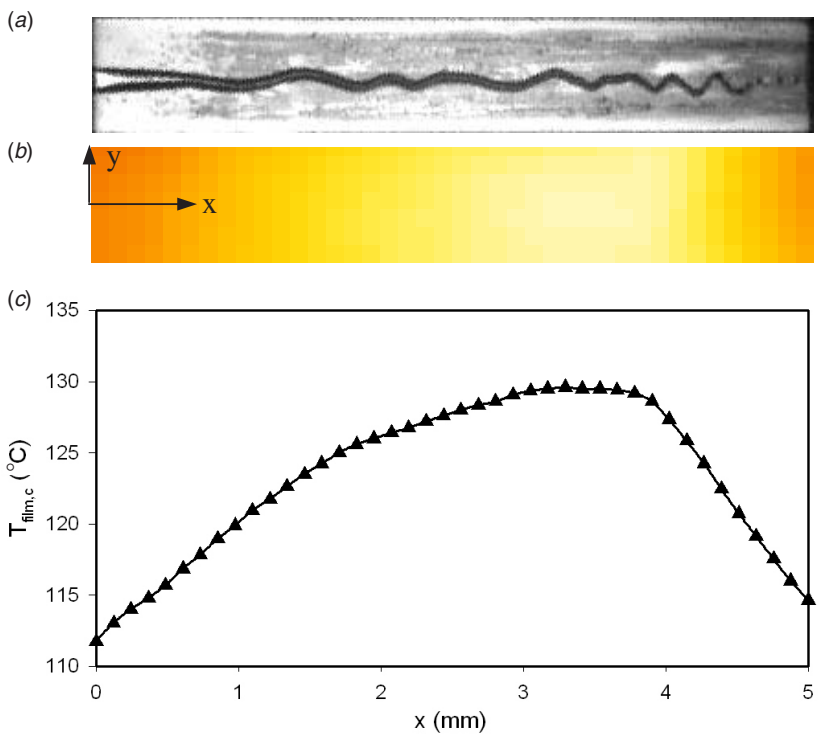

Figure 6. Flow pattern image (*a*), IR image showing the bottom heating surface temperatures (*b*) and the heating surface temperatures at $y = 0$ along the flow direction (*c*), for run 1.

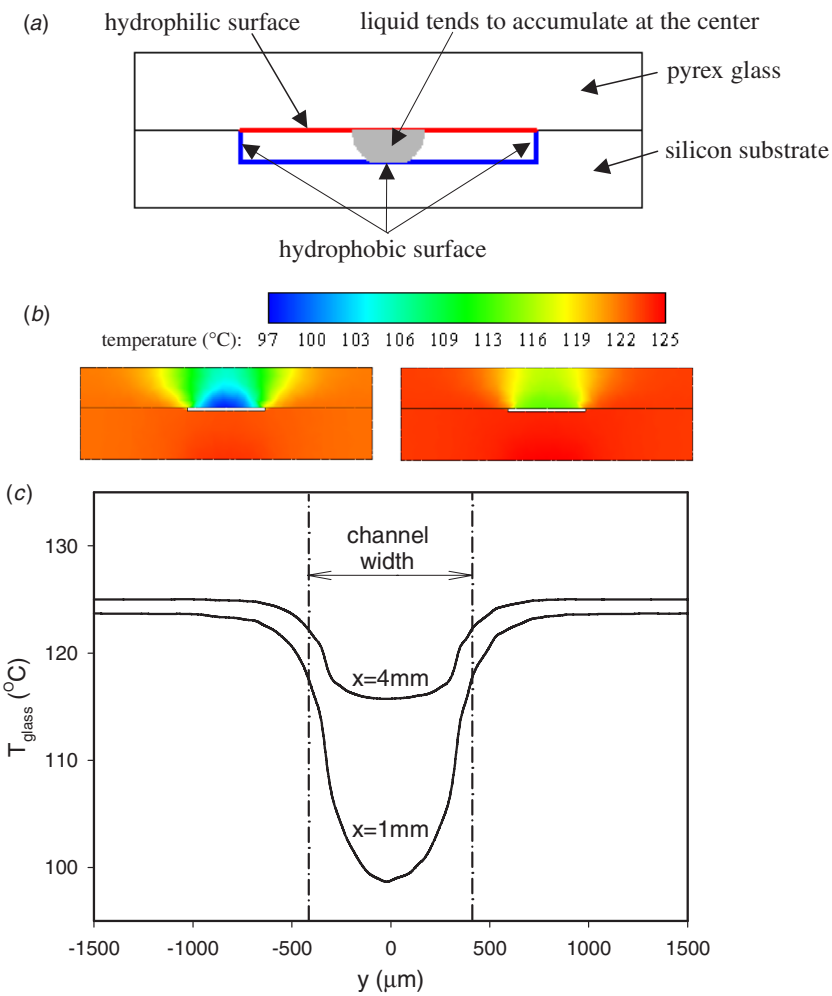

Figure 7. Central microchannel cross section showing the liquid population and surface wettability (*a*), cross-section temperatures of the glass cover and silicon substrate at $x = 1.0$ and 4.0 mm (*b*), and temperatures at the bonding surface including the top channel surface in the chip width direction at $x = 1.0$ and 4.0 mm (*c*), for run 1.

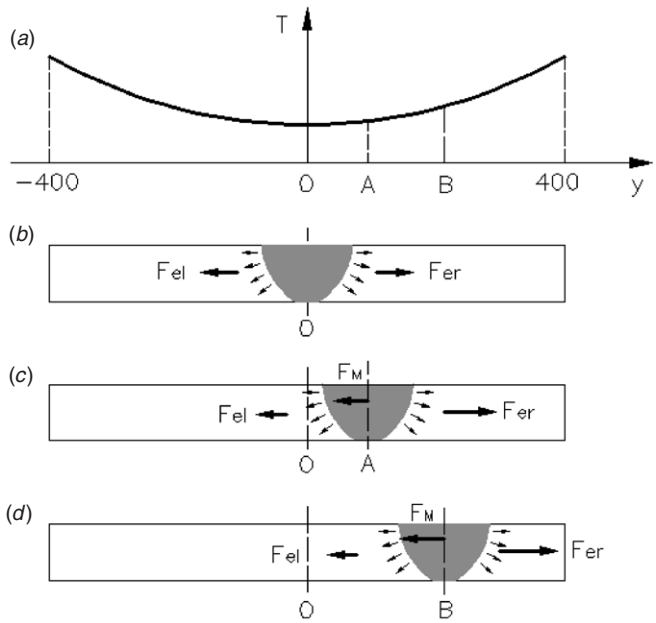

Figure 8. Mechanism for liquid rivulet deviation from the channel centerline.

rivulet from the channel centerline is explained in figure 8 for a cross section of the microchannel. As noted previously, the top glass surface of the microchannel is hydrophilic and has a lower temperature at the centerline of $y = 0$ than other locations (see figure 8(*a*)). Temperatures are increased away from the channel centerline. On the other hand, the bottom silicon surface is hydrophobic and has neglectable temperature gradient in the width direction. We analyze forces acting on the rivulet cross section per unit length. Because evaporation takes place at the vapor–liquid interface, two evaporation momentum forces are acted on the right and left rivulet interfaces, i.e. F_{er} and F_{el}, due to the mass exchange at the two interfaces. The evaporation momentum force is described by Kandlikar (2004). On the other hand, if the rivulet deviates from the channel centerline of $y = 0$, another force is acted on the rivulet due to the Marangoni effect by the temperature gradient in the channel width direction, which is called F_M. Such a force is always toward the channel centerline.

As shown in figure 8(*b*), initially, a quasi-stable state exists when the rivulet is exactly at the channel centerline of $y = 0$. The two evaporation momentum forces F_{el} and F_{er} are exactly equal but have opposite directions. A small disturbance causes the rivulet center to reach $y = y_A$; the disturbance may be

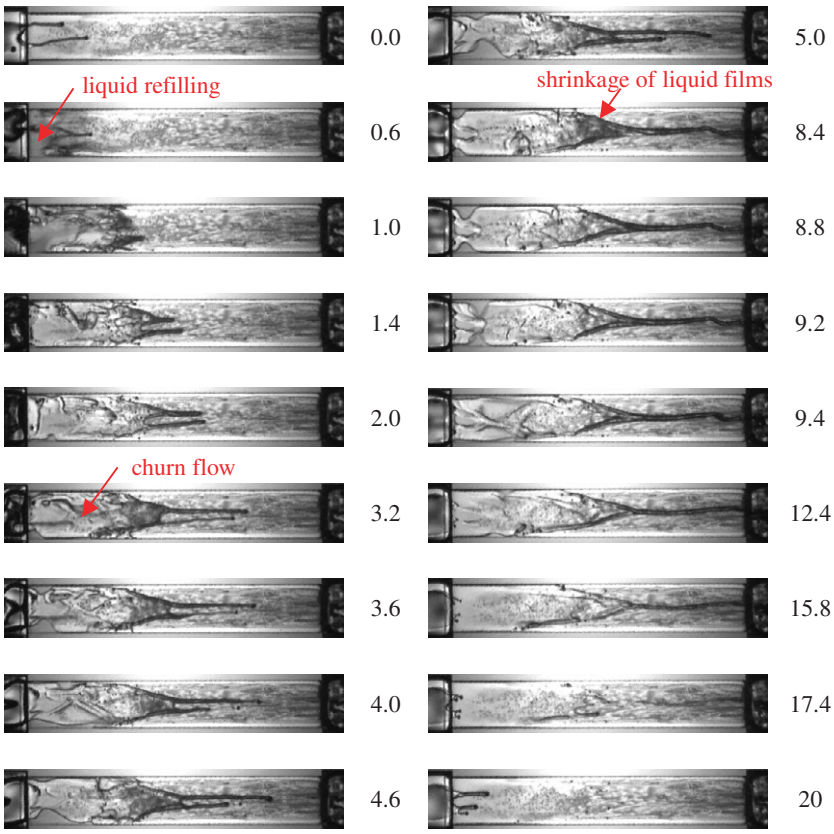

Figure 9. Periodic liquid rivulet ejection and receding process for run 4 (time scale is millisecond).

amplified if $F_{er} > F_{el} + F_M$, under which the rivulet further moves away from the channel centerline (see figure 8(*c*)). A new quasi-stable state exists when $F_{er} = F_{el} + F_M$ at $y = y_B$, as shown in figure 8(*d*). Such a state in figure 8(*d*) cannot last forever because a small disturbance also leads to the rivulet moving towards the channel centerline. We note that the rivulet has an axial flow velocity. Thus the zigzag pattern is observed. From the above analysis it is shown that the zigzag pattern is caused by the competition between the evaporation momentum forces at the two rivulet interfaces and the Marangoni force, depending on the temperatures and temperature gradients on the top glass cover surface. The zigzag pattern of the liquid rivulet is observed for run 1 at which both the temperatures and temperature gradients in the channel width direction are large. But the zigzag pattern is not observed for run 4, as will be seen in the later subsections.

Breakup of the liquid rivulet. As shown in figure 4, the breakup of the liquid rivulet takes place in the central microchannel downstream, corresponding to the negative temperature gradient along the flow direction there. The strong Marangoni force toward the axial coordinate snapped the rivulet to form a set of isolated droplets attached on the top microchannel surface (glass cover).

3.2. *Effect of outlet vapor qualities on the flow pattern*

Figure 9 describing run 4 shows the periodic rivulet ejection and receding pattern at the same pressure drop as that of figures 4–7 ($\Delta p = 20$ kPa), but the heat flux is decreased to 269.7 kW m^{-2}. At the same pressure drop, a decrease in heat flux results in the increase of the mass flux. Therefore, the mass flux is 43.9 kg m^{-2} s^{-1}, which is larger than that shown in figures 4–7. The boiling number is 0.0118 and the outlet equilibrium vapor quality is 1.95. Compared with the flow pattern shown in figure 4, the periodic rivulet ejection and receding pattern shown in figure 9 displays the following characteristics: (1) there is a churn flow section behind the shrinkage of the liquid films (fluid triangle), which does not appear in figure 4. The churn mixture of the vapor and liquid section may cover nearly half of the total central microchannel length instantaneously. (2) The liquid rivulet in front of the shrinkage of the liquid films is almost straight without showing an apparent zigzag pattern. (3) The breakup of the liquid rivulet in the central microchannel downstream does not occur.

Similarly, the large temperature gradient in the chip width direction (y-direction) on the glass cover surface is the reason behind the formation of the shrinkage of the liquid films (fluid triangle). However, because the boiling number is smaller than that for run 1, the maximum temperature at the back heating surface is decreased to 94 °C (see figure 3), which is significantly lower than those for run 1. Correspondingly, the temperature gradient in the microchannel width direction on the top glass cover surface is significantly decreased; thus the zigzag pattern of the rivulet is not apparent. Besides, the temperature gradient along the axial flow direction within the rivulet is decreased; thus the breakup of the rivulet in the central microchannel downstream is not apparent.

The cycle periods versus consecutive 35 cycles are shown in figure 10. Most cycles have a cycle period of about 20 ms,

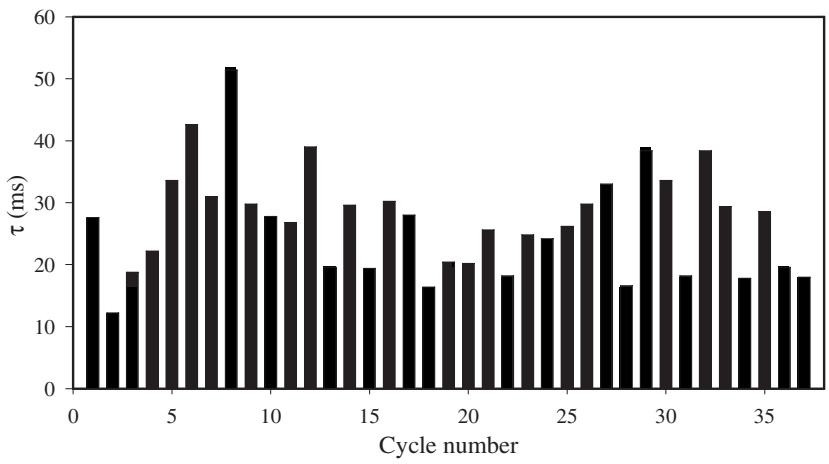

Figure 10. Cycle periods of the periodic rivulet ejection and receding process for consecutive cycles for run 4.

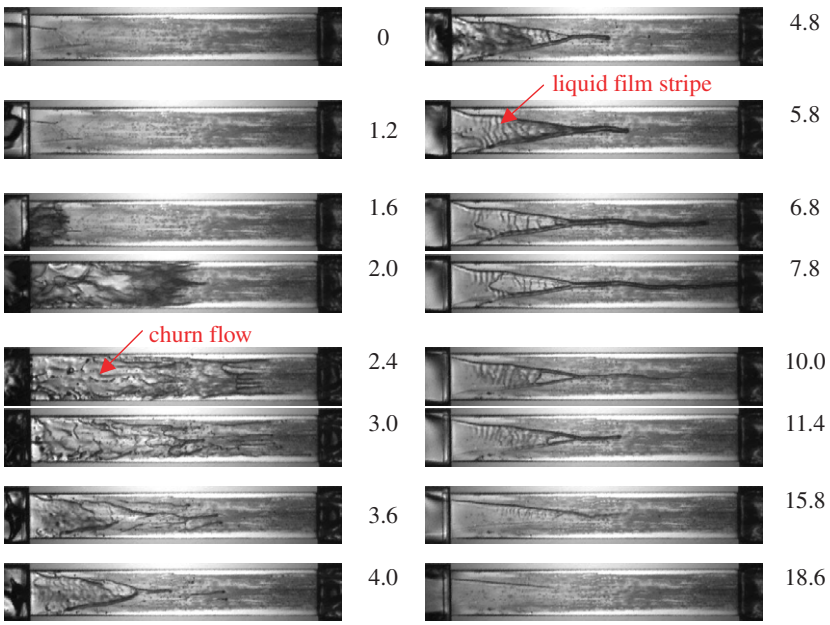

Figure 11. Periodic liquid rivulet ejection and receding process for run 6 (time scale is millisecond).

but the maximum cycle period reaches 50 ms and the minimum value is 12 ms. Compared with the cycle periods given in figure 5(*b*), the cycle period distribution behaves more uniformly.

It is a common knowledge that a higher pressure drop across the silicon chip leads to a larger mass flux in the microchannel. Figure 11 shows the periodic rivulet ejection and receding pattern for the pressure drop (Δp) of 30 kPa, with a mass flux G of 78.1 kg m^{-2} s^{-1} and a heat flux q of 363.0 kW m^{-2} (run 6 in table 2). Correspondingly, the outlet thermal equilibrium vapor quality is 1.47 and the boiling number Bo is 0.0089. The flow pattern for this run is similar to the one above, except that parallel liquid film stripes within the upstream fluid triangle (shrinkage of the liquid films) are observed. Figure 12 shows the cycle periods versus consecutive cycles. Slightly decreased cycle periods are observed than those shown in figure 5(*b*) for run 1 and figure 10 for run 4.

We explain the formation mechanism of liquid stripes inside the upstream fluid triangle in figure 13. The enlarged liquid stripes are shown in figure 13(*b*) focusing on the upstream fluid triangle area, with cross sections marked as A–A along the axial flow direction and B–B along the channel width direction. The liquid patterns in the two cross sections are shown in figures 13(*c*) and (*d*), respectively. The mixture flow in the fluid triangle is governed by the low capillary number. Along the flow direction (see figure 13(*c*)), the vapor velocity relative to the liquid phase is u_{fg}, producing an inertia force which is proportional to $\rho_v u_{fg}^2$ pushing the liquid phase in the downstream direction. Thus there is a viscous force between the top glass cover surface and the liquid phase, tending to spread the liquid film uniformly distributed on the top glass cover surface. On the other hand, the surface tension force tends to accumulate the liquid film locally on the top glass cover surface. The above two opposite effects can be quantified by the capillary number, i.e. $Ca = \mu_f u_{fg}/\sigma$. Given the values of $\mu_f = 2.37 \times 10^{-4}$ Pa s, $u_{fg} = 1$ m s^{-1} and $\sigma = 1.4 \times 10^{-2}$ N m^{-1} at the temperature of 373 K for acetone, the capillary number is 1.7×10^{-2}, which is quite small so that the

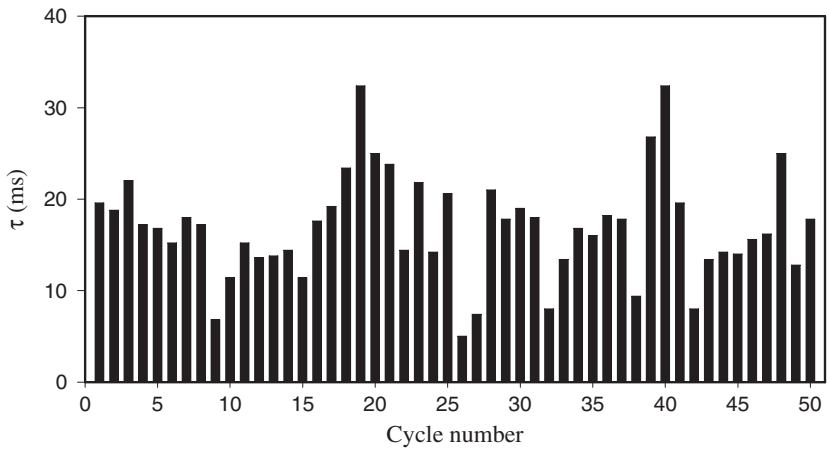

Figure 12. Cycle periods of the periodic rivulet ejection and receding process for consecutive cycles for run 6.

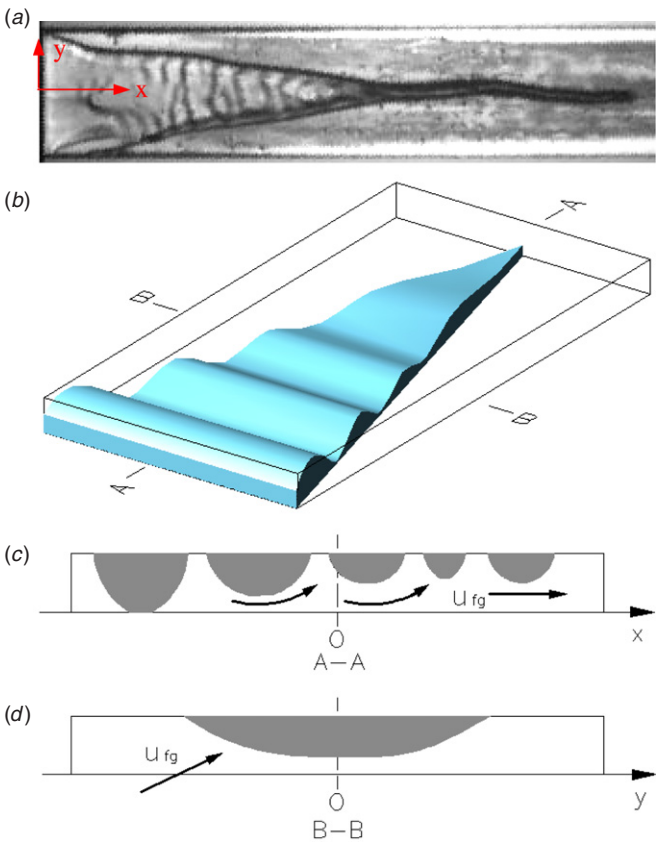

Figure 13. Liquid film stripes formation mechanism.

surface tension force controls the phase distribution, leading to the non-uniform distribution of the liquid film thickness on the top glass cover surface and the liquid stripes appear in the upstream fluid triangle.

4. Conclusions

We studied boiling heat transfer in a silicon microchannel heat sink. A top glass cover bonded with a bottom silicon substrate forms the silicon chip, with three consecutive parts of an inlet fluid plenum, a central microchannel and an outlet fluid plenum etched in the silicon substrate. The central microchannel had a length of 5000 μm with a cross section of 800 μm width and 30 μm depth. Acetone liquid was used as the working fluid. High outlet vapor qualities were dealt with here. The following conclusions can be drawn.

- The periodic liquid rivulet ejection and receding pattern appears in the timescale of milliseconds. The flow pattern consists of a fluid triangle (shrinkage of the liquid films) and a connected long liquid rivulet.
- The hydrophilic surface of the glass cover wets the liquid rivulet but the hydrophobic silicon surface has less contact area with the rivulet.
- The shrinkage of the liquid films in the central microchannel upstream is caused by the temperature gradient in the chip width direction at the top glass cover surface.
- Population of the long liquid rivulet near the microchannel centerline is also caused by the lower temperature at that location than elsewhere.
- The zigzag rivulet pattern in the central microchannel is caused by the competition of the two evaporation momentum forces at the right and left rivulet surfaces and the Marangoni force.
- Isolated droplets in the central microchannel downstream are formed by a negative temperature gradient along the flow direction there.
- Liquid stripes in the upstream fluid triangle are caused by the low capillary number. The viscous force tends to spread the liquid film uniformly distributed on the top glass cover surface, and the surface tension force tends to accumulate the liquid film locally on the glass surface. The small capillary number, which is on the order of 10^{-2}, leads to the non-uniform liquid film distribution on the top glass cover surface. Thus liquid stripes appear in the upstream fluid triangle.

Acknowledgments

This work was supported by the National Science Fund for Distinguished Young Scholars from the National Natural

Science Foundation of China (no 50825603) and the Natural Science Foundation of China (no 50776089).

References

Chen J C 1963 A correlation for boiling heat transfer to saturated fluids in convective flow *ASME paper reprint 63-HT-34 presented at 6th National Heat Transfer Conf. (Boston, 11–14 August 1963)*

Chen T and Garimella S V 2006 Measurements and high-speed visualizations of flow boiling of a dielectric fluid in a silicon microchannel heat sink *Int. J. Multiph. Flow* **32** 957–71

Garrity P T, Klausner J F and Mei R W 2007 A flow boiling microchannel evaporator plate for fuel cell thermal management *Heat Transfer Eng.* **28** 877–84

Hetsroni G, Mosyak A, Pogrebnyak E and Segal Z 2006 Periodic boiling in parallel microchannels at low vapor quality *Int. J. Multiph. Flow* **32** 1141–59

Howell J R and Menguc M P 1998 Radiation *Handbook of Heat Transfer* 3rd edn ed W M Rohsenow, J P Hartnett and Y I Cho (New York: McGraw-Hill)

Hsieh S S and Lin C Y 2009 Convective heat transfer in liquid microchannels with hydrophobic and hydrophilic surfaces *Int. J. Heat Mass Transfer* **52** 260–70

Kandlikar S G 2004 Heat transfer mechanisms during flow boiling in microchannels *Trans. ASME, J. Heat Transfer* **126** 8–16

Kandlikar S G, Kuan W K, Willistein D A and Borrelli J 2006 Stabilization of flow boiling in microchannels using pressure drop elements and fabricated nucleation sites *Trans. ASME, J. Heat Transfer* **128** 389–95

Kandlikar S G, Mizo V R, Cartwright M D and Ikenze E 1997 Bubble nucleation and growth characteristics in subcooled flow boiling of water *ASME Proc. of the 32nd National Heat Transfer Conf.* vol 4 pp 11–8 HTD-Vol.342

Kuo C J and Peles Y 2008 Flow boiling instabilities in microchannels and means for mitigation by reentrant cavities *Trans. ASME, J. Heat Transfer* **130** 072402

Maurya D K, Das S and Lahiri S K 2005 Silicon MEMS vaporizing liquid microthruster with internal microheater *J. Micromech. Microeng.* **15** 966–70

Muwanga R, Hassan I and MacDonald R 2007 Characteristics of flow boiling oscillations in silicon microchannel heat sinks *Trans. ASME, J. Heat Transfer* **129** 1341–51

Qu W L and Mudawar I 2004 Transport phenomena in two-phase microchannel heat sinks *Trans. ASME, J. Electron. Packag.* **126** 213–24

Tadrist L 2007 Review on two-phase flow instabilities in narrow spaces *Int. J. Heat Fluid Flow* **28** 54–62

Takahashi K, Weng J G and Tien C L 1999 Marangoni effect in microbubble systems *Microscale Thermophys. Eng.* **3** 169–82

Thome J R 2004 Boiling in microchannels, a review of experiment and theory *Int. J. Heat Fluid Flow* **25** 128–39

Wu H Y, Cheng P and Wang H 2006 Pressure drop and flow boiling instabilities in silicon microchannel heat sinks *J. Micromech. Microeng.* **18** 2138–46

Yaws C L 1999 *Chemical Properties Handbook* (New York: McGraw-Hill)

Zhang F, Zhao X, Geng J, Wu Y T and Zhang Z 2007 A new insight into Marangoni effect in non-isothermal falling films *Exp. Therm. Fluid Sci.* **31** 361–365

Zhang W, Xu J L and Liu G H 2008a Multi-channel effect of condensation flow in a micro triple-channel condenser *Int. J. Multiph. Flow* **34** 1175–84

Zhang W, Xu J L and Thome J R 2008b Periodic bubble emission and appearance of an ordered bubble sequence (train) during condensation in a single microchannel *Int. J. Heat Mass Transfer* **51** 3420–33